Experimental evaluation of common spacecraft data analysis techniques for reconnection region analysis in a laboratory plasma

Jongsoo Yoo[1] and Masaaki Yamada[1]

[1] A laboratory plasma is utilized to assess the effectiveness of several prominent spacecraft data analysis techniques. These include minimum variance analysis on the magnetic field (MVAB) and various boundary-crossing time analyses (BCTA) such as the constant velocity approach (CVA), constant thickness approach (CTA), and minimum thickness variance (MTV). Magnetic field data from measurement points that resemble the formation of multispacecraft flying though a reconnecting current sheet is used to check MVAB and BCTA to deduce a proper normal vector. Results from each method are compared to the values measured by 2-D magnetic probe arrays. We examine discharges with a two-dimensional (2-D) X-line structure as well as cases in which a flux rope forms within the layer. All discharges are in a two-fluid regime in which electrons are magnetized but ions are not. We conclude that CVA with four sample measurement points forming a tetrahedron generates a reasonable unit normal vector $\hat{\mathbf{n}}$, relative velocity along the normal vector V_n, and current sheet thickness δ_{CS} for all of the tested cases. Unlike CVA, both CTA and MTV sometimes generate V_n and δ_{CS} that are different from the measured values, which indicates that CTA and MTV are sensitive to changes in the current sheet thickness. CTA is, however, successful at estimating $\hat{\mathbf{n}}$. MVAB, on the other hand, often fails to predict a proper normal direction. This is because the reconnecting neutral sheet fundamentally contains 2-D or 3-D structures. MVAB, however, does determine the direction along the reconnecting magnetic field that is close to the real magnetic geometry. Based on these observations, we suggest a hybrid procedure for determining a local coordinate system for data from four spacecraft passing through a reconnecting current sheet.

1. Introduction

[2] For many decades, satellite measurements have been employed to understand the complex nature of the magnetic fields surrounding Earth. These measurements have revealed the presence of magnetic reconnection throughout Earth's magnetosphere [e.g., *Paschmann et al.*, 1979; *Phan et al.*, 2000; *Øieroset et al.*, 2001; *Phan et al.*, 2006; *Angelopoulos et al.*, 2008]. During the past dozen years, the role of magnetic reconnection has been studied in detail through a combined effort that includes numerical simulations, dedicated laboratory plasma experiments, and direct observations from spacecraft [*Yamada et al.*, 2010]. As a result of this effort, it is now recognized that two-fluid effects resulting from the different behavior of ions and electrons in the reconnection layer play a key role in collisionless reconnection [*Yamada*, 2007; *Zweibel and Yamada*, 2009; *Mozer et al.*, 2002; *Vaivads et al.*, 2004]. In order to further study two-fluid effects in the magnetosphere, the Magnetospheric MultiScale (MMS) mission will be launched in 2014 to explore spatial scales down to the electron inertial length (c/ω_{pe}), a measurement regime which is critical to obtain a complete understanding of collisionless reconnection.

[3] One of the foremost challenges of using spacecraft to study reconnection is properly identifying the local magnetic field geometry. Because the number of spacecraft is limited, the spatial profile of the plasma has to be inferred from the time series of physical quantities such as the magnetic field and electric field, typically using at most four locations. Several analysis methods have been developed to address this challenging problem. Classical minimum variance analysis on magnetic field data (known as MVAB) [*Sonnerup and Cahill*, 1967] has been employed for many spacecraft data analyses [e.g., *Øieroset et al.*, 2001]. Alternatively, maximum variance analysis of electric field data (MVAE) [*Sonnerup et al.*, 1987; *Paschmann et al.*, 1990] or the

---

[1]Center for Magnetic Self-Organization in Laboratory and Astrophysical Plasmas, Princeton Plasma Physics Laboratory, Princeton University, Princeton, New Jersey, USA.

Corresponding author: J. Yoo, Center for Magnetic Self-Organization in Laboratory and Astrophysical Plasmas, Princeton Plasma Physics Laboratory, Princeton University, Princeton, NJ 08543, USA. (jyoo@pppl.gov)

Faraday residue method [*Terasawa et al.*, 1996; *Khrabrov and Sonnerup*, 1998a] can be employed if electric field measurements are also available. These variance analysis methods (MVAB, MVAE, and the Faraday residue method) are capable of identifying a vector normal to the reconnection current layer using data from a single spacecraft.

[4] If multiple spacecraft are available, more information on the reconnection layer can be obtained via boundary crossing time analysis (BCTA). For example, BCTA was used to estimate the normal component of the relative velocity of a boundary V_n and current sheet thickness δ_{CS} for data from ISEE 1 and ISEE 2 [*Berchem and Russell*, 1982]. Similar analysis has been carried out on data from 16 crossings of Earth's magnetopause by the spacecraft AMPTE/UKS and IRM [*Bauer et al.*, 2000]. In these studies, which had only two spacecraft, the normal vector $\hat{n}$ is determined by the single-spacecraft variance analyses such as MVAB. When four spacecraft are available, however, $\hat{n}$ can be obtained with better accuracy by BCTA without the use of single-spacecraft techniques [*Russell et al.*, 1983]. This is why BCTA has been widely used for data from the four-spacecraft Cluster mission [*Vaivads et al.*, 2004; *Eastwood et al.*, 2005; *Khotyaintsev et al.*, 2006; *Eastwood et al.*, 2007; *Retinò et al.*, 2007, 2008; *Rosenqvist et al.*, 2008].

[5] For a detailed study of reconnection, more information on the magnetic geometry is needed; knowing the direction normal to the current sheet is not enough. In particular, key physical parameters such as the reconnection rate cannot be estimated without differentiating two tangential directions: the out-of-plane direction and the direction of the reconnecting magnetic field. In some cases, the MVAB or MVAE techniques successfully separate all three principal axes that naturally form a coordinate system, from which the full local magnetic geometry can be inferred. However, when the variances along two principal axes are similar, they cannot reconstruct the magnetic geometry properly. In attempt to address these shortcomings, *Mozer and Retinò* [2007] combined MVAB and MVAE to find a rotation matrix transforming the GSE coordinate system into the magnetopause frame. They noticed that MVAB best finds the direction of the reconnecting magnetic field component which is the maximum varying component, while MVAE best locates the maximum varying normal electric field component. In this study, however, the validity of results from the combined procedure could not be checked since the actual magnetic geometry is not known.

[6] For a quantitative test of spacecraft analysis techniques, we need to acquire similar types of data from a known magnetic geometry. A well-controlled, well-diagnosed current sheet in the Magnetic Reconnection Experiment (MRX) provides a unique opportunity to perform such a quantitative test. In particular, the current sheet is swept over the stationary probes via internal pulsed coils. This situation is very similar to the space measurements in which the current sheet moves with respect to spacecraft. This plasma "jogging" experiment is carefully designed and performed so that we can test these methods in the plasma in which we monitor evolution of the profile of the magnetic field measured by multiple magnetic probe arrays.

[7] With the use of data from the plasma jogging experiment, we present a detailed and thorough laboratory test of two of the methods mentioned above, minimum variance analysis of the magnetic field and boundary-crossing time analysis, in a collisionless reconnection layer. First, both methods are tested to produce proper normal vectors. Second, three different versions of BCTA (CVA, CTA, and MTV) are used to estimate V_n and the current sheet thickness δ_{CS} and they are compared to measured values in order to evaluate the effectiveness of each method. Third, we compare the results from MVAB and BCTA and present a hybrid procedure for determining a local magnetic geometry based on elements of both MVAB and BCTA which can be used by any four-spacecraft mission such as Cluster and the Magnetospheric MultiScale (MMS) mission. It should be noted that we do not perform MVAE or the Faraday residual analysis because we do not currently have sufficient electric field measurement capabilities.

2. Experimental Apparatus

[8] For more than a decade, the Magnetic Reconnection Experiment has been dedicated to study of magnetic reconnection in a controlled laboratory environment. In MRX plasmas, the MHD criteria ($S \gg 1$, $\rho_i \ll L$, where S is the Lundquist number; ρ_i is the ion gyroradius; L is the system scale length) are satisfied in the bulk of the plasma [*Yamada et al.*, 1997]. Figure 1 shows an R-Z cross section of the MRX vacuum vessel for this experimental campaign. The two gray circles are "flux cores" that each contain two independent coils: a poloidal field (PF) coil and a toroidal field (TF) coil [*Yamada et al.*, 1981]. The PF coils generate the X-line geometry at the middle of the MRX device and drives magnetic reconnection, while the TF coils inductively create the plasma around the flux cores. As the PF coil current ramps down, the magnetic flux is pulled toward the flux cores and a current sheet forms that is elongated along the Z direction (indicated in orange in Figure 1). In this phase, the initial out-of-plane magnetic field that is produced during the plasma formation phase becomes negligible compared to the reconnecting magnetic field such that anti-parallel reconnection is achieved. The entire process of plasma formation and magnetic reconnection is monitored by 2-D magnetic probe arrays located every 3 cm from $Z = -9$ cm to 9 cm and electrostatic probes such as Langmuir probes and Mach probes. The maximum radial resolution of the magnetic arrays is 0.6 cm and the radial coverage is 16 cm. Data is acquired every 0.4 μs.

[9] In this experimental campaign, another set of coils (red circles in Figure 1) called the shaping field (SF) coils is used to drive the plasma radially inward. This accelerated motion of the current sheet is called "jogging." The advantage of this jogging experiment is that a simulated "satellite" data set can be obtained when the current sheet region is swept past a stationary probe with a predetermined velocity and angle. Figure 2 illustrates radial profiles of B_Z during the quasi-steady period of a single discharge of the MRX jogging experiment. Asterisks stand for measured data and solid lines are results of fitting the radial profiles into a Harris-sheet type function [*Harris*, 1962], $\sim\tanh((R - R_0)/\delta)$ [*Ji et al.*, 1999]. The jogging speed of the current sheet can be controlled by firing the SF coils with various voltages. Figure 3 shows time profiles of the current sheet location with various SF firing voltages. The SF coils are activated just before the quasi-steady period of the MRX plasma. Shortly after they are fired, the current sheet moves in radially. The location of the current sheet is from the Harris fitting. The jogging speed increases almost linearly with the firing voltage. In the
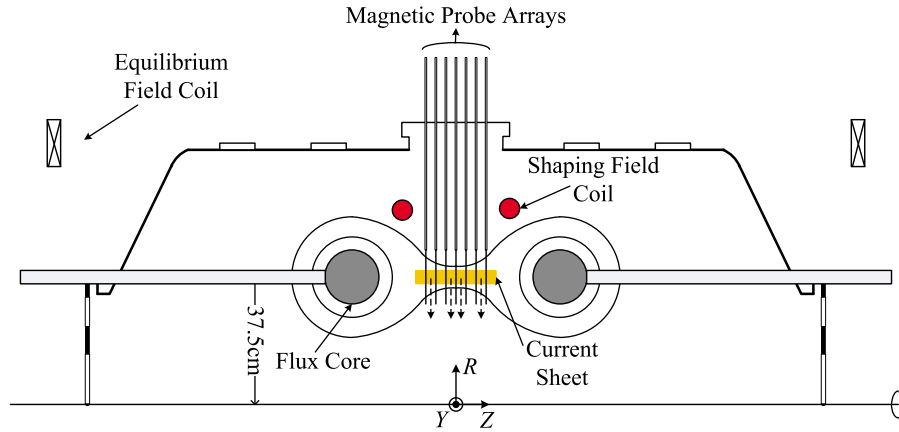
Figure 1. Cross section of the MRX vacuum chamber. The gray circles indicate flux cores in which there are two sets of coils: poloidal field (PF) coils and toroidal field (TF) coils. PF coils produce the X-line geometry and drive reconnection. The red circles show the position of the shaping field (SF) coils which are used to accelerate the motion of the current sheet radially inward.

discharge presented in Figure 2, the current sheet moves about 3.5 cm over 6 μs, yielding a speed of 5.8 km/s, which is about one order of magnitude lower than the Alfvén velocity based on upstream plasma parameters ($n_e = 2$–5×10^{13} cm^{-3} and $|\mathbf{B}| = 200$–250 Gauss). Every discharge presented in this paper has a similar radial speed (5–6 km/s).

3. Minimum Variance Analysis on Magnetic Field

3.1. Description of Method

[10] Following *Mozer and Retinó* [2007], the following coordinate system, which is similar to the GSE system for subsolar reconnection, is used throughout this paper: x is normal to the current sheet, y is along the out-of-plane direction, and z is in the direction of the reconnecting magnetic field. The corresponding local Cartesian coordinates for reconnection during the quasi-steady period in MRX are R, Y, and Z respectively [*Yamada et al.*, 1997].

[11] The theory behind MVAB can be found in the literature [*Sonnerup and Cahill*, 1967; *Sonnerup and Scheible*, 1998] but we briefly describe it here. The fundamental assumption of MVAB is that the boundary is one-dimensional. With this assumption, the normal component of the magnetic field remains constant during the satellite crossing. In reality, however, due to 2-D or 3-D structures, temporal variations, and/or noise, the normal component undergoes finite changes. The basic idea of MVAB is that the direction along which the magnetic field component varies least is the most probable direction for the normal vector $\hat{\mathbf{n}}$. Such a unit vector $\hat{\mathbf{n}}$ can be
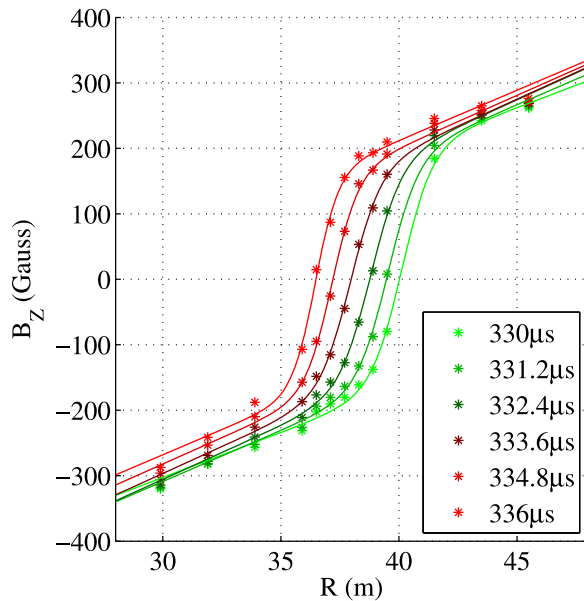

Figure 2. Radial profiles of B_Z every 1.2 μs during the quasi-steady period of a single discharge, measured by the magnetic probe array at $Z = 0$. Asterisks stand for measured data and the solid lines come from fitting the data to a Harris function, $\sim \tanh((R - R_0)/\delta)$. The current sheet moves in with a relatively well-maintained structure at about 5.8 km/s.
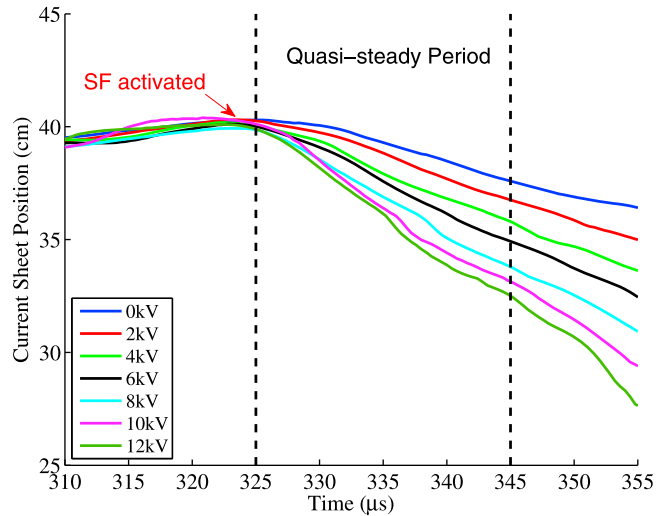
Figure 3. Current sheet motion as a function of the firing voltage for the SF coils. Shortly after the SF coils are activated, the current sheet starts to move in. The jogging speed of the current sheet is proportional to the firing voltage. Two black dashed lines indicate the quasi-steady period of the MRX plasma.

found by computing eigenvectors of the symmetric matrix $\mathbf{M}$ defined by

$$M_{\mu\nu} = \langle B_\mu B_\nu \rangle - \langle B_\mu \rangle \langle B_\nu \rangle, \tag{1}$$

where B_μ and B_ν are components of the measured magnetic field based on a Cartesian coordinate system. For MRX data, these components are B_R, B_Y, and B_Z. Since the magnetic variance matrix $\mathbf{M}$ is symmetric, three eigenvalues λ_1, λ_2, and λ_3 in order of increasing magnitude are real, and their corresponding normalized eigenvectors $\mathbf{u}_1$, $\mathbf{u}_2$, and $\mathbf{u}_3$ are orthogonal. Mathematically, each eigenvalue equals the variance along the corresponding eigenvector. Thus, if a spacecraft encounters the current sheet and passes though it, the normalized eigenvector $\mathbf{u}_1$ that has the minimum variance is a natural choice for the unit normal vector $\hat{\mathbf{n}}$, or $\hat{\mathbf{x}}$. Because magnetic field component along the direction of the reconnecting magnetic field B_z varies most across the layer, $\mathbf{u}_2$ and $\mathbf{u}_3$ are parallel to $\mathbf{y}$ and $\mathbf{z}$ respectively.

[12] The size of the data segment, M, is chosen by checking that the results of MVAB are stationary. If the basic assumption of MVAB is satisfied, i.e. if the boundary is 1-D, MVAB is independent of the number of data points. This stationary property of MVAB is not guaranteed in real data. If M is too small or too large, results from MVAB can be different from those with intermediate data segments [*Sonnerup and Scheible*, 1998]. Thus, the stationarity of MVAB must be checked to make sure the nested data segment is within the intermediate, or "plateau" region. As M increases, the average magnetic field along the normal vector from MVAB $\langle \mathbf{B} \rangle \cdot \hat{\mathbf{n}}$ remains nearly unchanged, indicating a plateau region as shown in Figure 6a. The number of data points M is chosen such that the data segment is in the plateau region.

[13] To summarize the procedure of determining local coordinates by MVAB, a proper span of magnetic field data centered at the middle of the current sheet must be chosen. Then, the magnetic variance matrix $\mathbf{M}$ is constructed from the data and eigenvalues and eigenvectors of $\mathbf{M}$ are computed. The normalized eigenvector corresponding to the smallest eigenvalue determines the normal direction $\hat{\mathbf{x}}$, i.e., $\hat{\mathbf{x}} = \pm\mathbf{u}_1$. The other two eigenvectors $\mathbf{u}_2$ and $\mathbf{u}_3$ define $\hat{\mathbf{y}}$ and $\hat{\mathbf{z}}$. Proper signs should be chosen to make sure $\hat{\mathbf{z}} = \hat{\mathbf{x}} \times \hat{\mathbf{y}}$. Then, the transformation of values in the original cartesian coordinates (R, Y, Z) to those in (x, y, z) is given by

$$\begin{pmatrix} x \\ y \\ z \end{pmatrix} = \begin{pmatrix} \hat{\mathbf{x}} \\ \hat{\mathbf{y}} \\ \hat{\mathbf{z}} \end{pmatrix} \begin{pmatrix} R \\ Y \\ Z \end{pmatrix}. \tag{2}$$

3.2. MVAB Results and Analysis

[14] Data from the MRX jogging experiment provides a good opportunity to test MVAB since the full 2-D (or 3-D) magnetic field geometry is independently measured. Whether MVAB generates a proper normal vector can be easily checked by comparing the local magnetic geometry predicted by MVAB with the measured global geometry.

[15] Figure 4 shows the time evolution of 2-D profiles of the current density J_Y with contours of the poloidal magnetic

flux $\Psi \equiv \int_0^R 2\pi R' B_Z(Z, R', t) dR'$ and the out-of-plane magnetic field B_Y measured by the 2-D magnetic probe arrays during the quasi-steady period of a typical MRX jog discharge. The right column shows the quadrupolar B_Y structure moving in radially with temporal changes mainly due to the TF coil current ringing [*Ren et al.*, 2008]. The radial motion of the current sheet is shown in the left column. The current sheet structure is well-maintained and moves in with the quadrupolar B_Y. The layer clearly has 2-D structures: J_Y varies along Z and the $B_Z = 0$ boundary indicated by red dashed lines is slightly kinked in the $R - Z$ plane, especially at $t = 340$ μs. However, the direction normal to the current sheet is generally along $\mathbf{e}_R$, the unit vector for R, as the curvature of the $B_Z = 0$ boundary remains small. The angle between the local vector normal to the boundary and $\mathbf{e}_R$ is less than 5 degrees. Furthermore, toroidal asymmetry is monitored by an additional magnetic probe at $Y = -9$ cm and is found to be fairly negligible for this plasma. Therefore, the rotation matrix that transforms from (R, Y, Z) into (x, y, z) coordinates for this discharge should have diagonal terms close to unity and off-diagonal terms close to zero. In other words, $\hat{\mathbf{x}} \approx \mathbf{e}_R$, $\hat{\mathbf{y}} \approx \mathbf{e}_Y$, and $\hat{\mathbf{z}} \approx \mathbf{e}_Z$.

[16] As shown in Figure 5, data from four different measurement points ($Z = 0, 3, 6, 9$ cm; $R = 36.7$, $Y = 0$ for all) of the same discharge is used to test MVAB. At $Z = 0$, in the right vicinity of the X point, only the reconnecting magnetic field B_Z varies significantly as shown in Figure 5c. In this case, variance of B_R is comparable to that of B_Y and the normal vector generated by MVAB becomes a mixture of $\mathbf{e}_R$ and $\mathbf{e}_Y$. The rotation matrix predicted by MVAB for this example is

$$\begin{pmatrix} x_1 \\ y_1 \\ z_1 \end{pmatrix} = \begin{pmatrix} 0.3576 & 0.9314 & 0.0682 \\ -0.9338 & 0.3560 & 0.0349 \\ 0.0082 & -0.0762 & 0.9971 \end{pmatrix} \begin{pmatrix} R \\ Y \\ Z \end{pmatrix}, \tag{3}$$

where the subscript 1 is added to avoid confusion and to emphasize that these are just a 'suggested' coordinate system by MVAB at the given location. The normal vector is $0.3576\mathbf{e}_R + 0.9314\mathbf{e}_Y + 0.0682\mathbf{e}_Z$, which is closer to $\mathbf{e}_Y$ than to the reference normal $\mathbf{e}_R$. Even though three eigenvalues of $\mathbf{M}$ are well-separated as shown in Figure 5c', the normal vector does not reflect the real magnetic geometry. The smallest and intermediate eigenvalues are often degenerate ($\lambda_1 \sim \lambda_2$) at $Z = 0$ in other discharges. However, MVAB predicts the direction of the reconnecting field well ($\hat{\mathbf{z}}_1 \simeq \mathbf{e}_Z$).

[17] At $Z = 3$ cm, the quadrupolar out-of-plane field starts to play a role. While B_R remains small, B_Y changes moderately as shown in Figure 5d. As a result, the three eigenvalues are well-separated and the unit vectors suggested by MVAB reflect the magnetic geometry. The coordinate system determined by MVAB is usually best at $Z = \pm 3$ cm for MRX jogging experiment data. The transformation matrix predicted by MVAB at this location is

$$\begin{pmatrix} x_2 \\ y_2 \\ z_2 \end{pmatrix} = \begin{pmatrix} 0.9976 & 0.0630 & 0.0297 \\ -0.0687 & 0.9601 & 0.2712 \\ -0.0115 & -0.2726 & 0.9621 \end{pmatrix} \begin{pmatrix} R \\ Y \\ Z \end{pmatrix}. \tag{4}$$
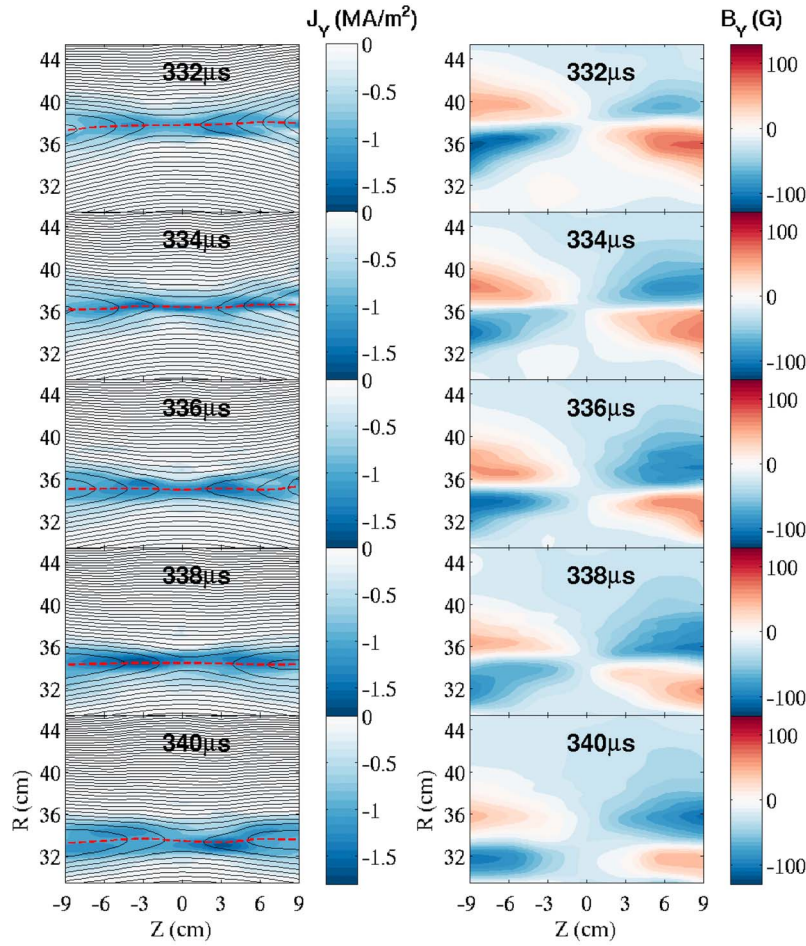
Figure 4. Data from 2-D magnetic probe arrays during the quasi-steady period of the MRX jog experiment discharge 114338 is shown. (left) Colors demonstrate the profile of the current density J_Y, while the black lines represent contours of the poloidal flux Ψ. The red dashed lines indicate the location of $B_Z = 0$ boundary which agrees with the current sheet location from the Harris fitting. (right) Contour plots show the time evolution of the out-of-plane magnetic field B_Y every 2 μs. Because of the time-varying TF current, the overall shape of the quadrupole structure undergoes temporal changes. The current sheet moves in radially together with the quadrupolar B_Y structure with a speed of $\sim$6 km/s.

Here, the normal vector from MVAB is very close to the reference normal. It is worth noting that $\hat{\mathbf{z}}_2$ has been degraded as it picks up a sizable $\mathbf{e}_Y$ component, which means the Hall field is considered a part of the reconnecting field by MVAB. The predicted out-of-plane direction $\hat{\mathbf{y}}_2$ also has a considerable $\mathbf{e}_Z$ component. Thus, as shown in Figure 5d′, the quadrupolar component of B_{y2} is weakened after the coordinate transformation. This tendency is enhanced further downstream, so that the transformed out-of-plane magnetic field component B_y is significantly contaminated by the other two components and frequently loses its bipolar shape (See Figures 5e′ and 5f′). This could be one of the reasons why a clear quadrupolar structure has rarely been identified in space [Mozer and Retinò, 2007].

[18] At $Z = 6$ cm, the variation in B_R becomes non-negligible because of the 2-D structure of the reconnection geometry. For most cases, this leads to a degenerate condition with $\lambda_1 \sim \lambda_2$, making $\hat{\mathbf{x}}_3$ and $\hat{\mathbf{y}}_3$ meaningless. The suggested transformation for this example is

$$\begin{pmatrix} x_3 \\ y_3 \\ z_3 \end{pmatrix} = \begin{pmatrix} 0.7990 & -0.5677 & -0.1984 \\ 0.5927 & 0.6876 & 0.4195 \\ -0.1017 & -0.4528 & 0.8858 \end{pmatrix} \begin{pmatrix} R \\ Y \\ Z \end{pmatrix}. \quad (5)$$

$\hat{\mathbf{z}}_3$ is further deviated from $\mathbf{e}_Z$ and both $\hat{\mathbf{x}}_3$ and $\hat{\mathbf{y}}_3$ do not reflect the real magnetic geometry. Similar trends continue at $Z = 9$ cm where MVAB generates the following coordinate transformation:

$$\begin{pmatrix} x_4 \\ y_4 \\ z_4 \end{pmatrix} = \begin{pmatrix} 0.8542 & -0.5036 & -0.1291 \\ 0.4888 & 0.6935 & 0.5293 \\ -0.1770 & -0.5152 & 0.8386 \end{pmatrix} \begin{pmatrix} R \\ Y \\ Z \end{pmatrix}. \quad (6)$$
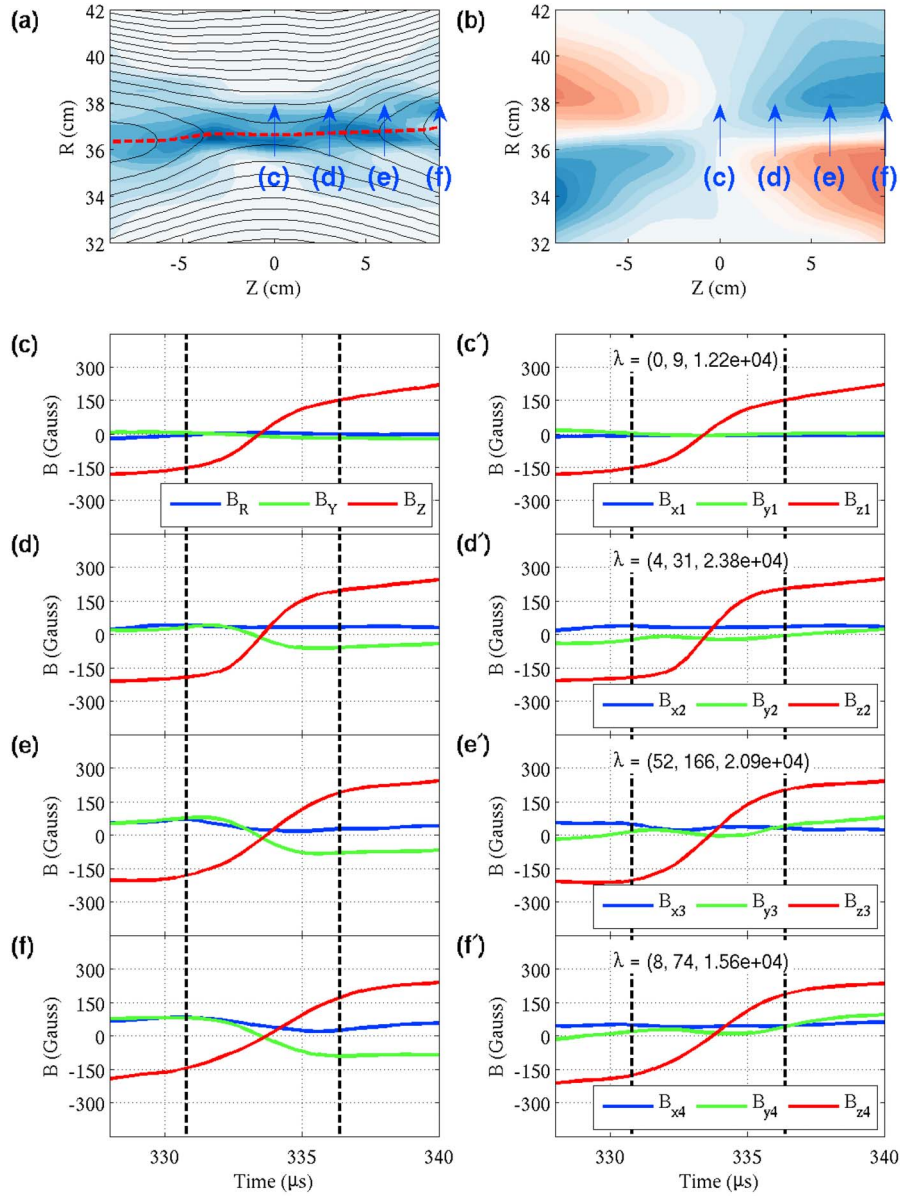
Figure 5. (a) 2-D profile of J_Y with contours of Ψ of the discharge 114338 at the time the current sheet is close to the sample measurement points. (b) 2-D profile of B_T. Color scales are the same as in Figure 4. The arrows indicate the data range used for MVAB. Magnetic field data at $(R, Z) =$ (c) (36.7, 0), (d) (36.7, 3), (e) (36.7, 6), and (f) (36.7, 9) ($Y = 0$ for all), respectively around the time the current sheet passes. Data between dashed black lines is used for MVAB. (c′–f′) Profiles in (x, y, z) coordinates suggested by MVAB. Three eigenvalues (λ) of the matrix **M** are shown inside of each panel. The out-of-plane magnetic field (B_Y) loses the bipolar shape after the coordinate transform by MVAB.

In this example, the suggested normal vector is again closer to $-\mathbf{e}_Y$ than to $\mathbf{e}_R$, which does not agree with the real magnetic geometry.

[19] To confirm that the above disagreement between the normal vectors from MVAB and the measured magnetic geometry is not due to measurement noise, we perform error estimations following *Khrabrov and Sonnerup* [1998b] where errors associated with random noise in minimum/

maximum variance analysis are analytically derived. In the reference, the angular uncertainty is given by

$$\left|\Delta\phi_{ij}\right| = \left|\Delta\phi_{ji}\right| = \sqrt{\frac{\lambda_1}{(M-1)}\frac{\left(\lambda_i + \lambda_j - \lambda_1\right)}{\left(\lambda_i - \lambda_j\right)^2}}, \quad i \neq j, \quad (7)$$
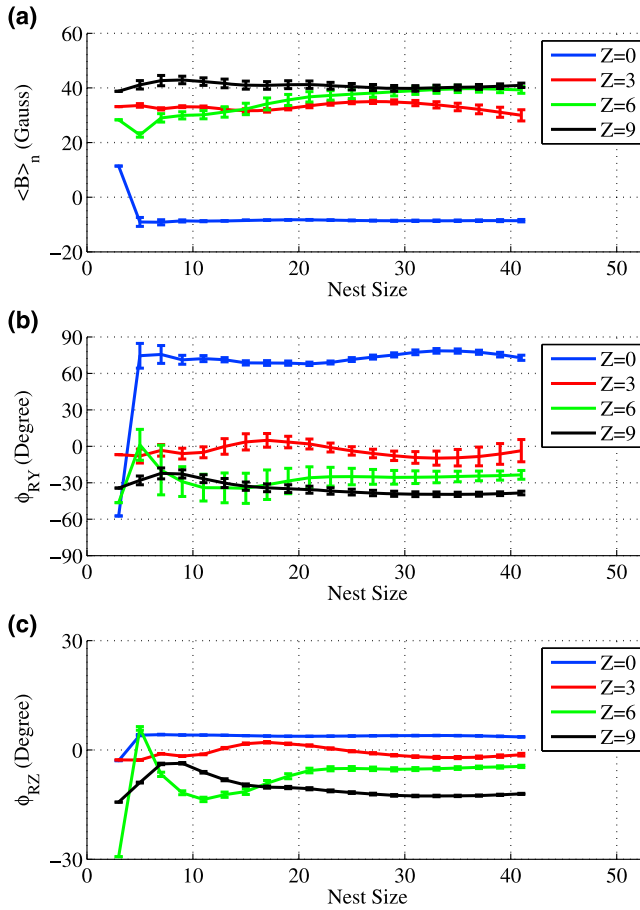
Figure 6. (a) Average magnetic field component along the suggested normal vector $\mathbf{u}_1$ from MVAB ($\langle\mathbf{B}\rangle_n \equiv \langle\mathbf{B}\rangle \cdot \hat{\mathbf{u}}_1$) as function of the nest size M. Error bars are computed by equation (8). (b) Angle between $\mathbf{u}_1$ and the reference normal vector $\mathbf{e}_R$ in the R-Y plane (ϕ_{RY}) as function of M. Except at $Z = 3$, the angle ϕ_{RY} is not close to zero for any value of M. (c) Angle between $\mathbf{u}_1$ and the reference normal vector $\mathbf{e}_R$ R-Z plane (ϕ_{RZ}) as function M. The angle ϕ_{RZ} is usually smaller than ϕ_{RY} since MVAB well-separates the direction of the reconnecting magnetic field from others.

where $|\Delta\phi_{ij}|$ is the angular uncertainty of eigenvector $\mathbf{u}_i$ in the direction of $\mathbf{u}_j$. The combined statistical error estimate for $\langle\mathbf{B}\rangle_n \equiv \langle\mathbf{B}\rangle \cdot \mathbf{u}_1$ is [*Sonnerup and Scheible*, 1998]

$$|\Delta\langle\mathbf{B}\rangle \cdot \mathbf{u}_1| = \sqrt{\frac{\lambda_1}{M-1} + (\Delta\phi_{12}\langle\mathbf{B}\rangle \cdot \mathbf{u}_2)^2 + (\Delta\phi_{13}\langle\mathbf{B}\rangle \cdot \mathbf{u}_3)^2},$$
(8)

where the first term inside of the square root comes from the uncertainty in the average magnetic field associated with the variance λ_1.

[20] Figure 6 shows the results of the error estimates with $M = 3$–41 for the same data used for MVAB in Figure 5. Error bars in this figure are computed by the above equations. The estimated statistical errors in $\langle\mathbf{B}\rangle$ are generally small as shown in Figure 6a, which is expected since the signal-to-noise ratio of MRX magnetic data is small. Figures 6b and 6c show the angle between the normal vector from MVAB, $\mathbf{u}_1$, and the reference normal vector, $\mathbf{e}_R$, in the

R-Y plane (ϕ_{RY}), and in the R-Z plane (ϕ_{RZ}) as a function of the nest size, M. When the normal vector from MVAB agrees with the measured global magnetic geometry, both ϕ_{RY} and ϕ_{RZ} are close to zero. Except at $Z = 3$ cm, ϕ_{RY} and ϕ_{RY} are not close to zero and statistical errors do not account for the difference. Therefore, the disagreement of the results from MVAB with the global magnetic geometry does not come from random noise. A possible explanation of the reason for frequent failures of MVAB based on an idealized 2-D X-line geometry is presented in section 5.

[21] MVAB is also tested in a discharge with a time-varying reconnection geometry. As shown in Figure 7a, a clear O-point is developed and ejected downstream. This O-point is associated with very high local current density and is believed to have a 3-D structure [*Dorfman*, 2011], so we describe this feature as a "flux rope" to emphasize its 3-D nature even though it is not accompanied with a sizable guide field. MVAB is conducted for data from the measurement point at $(R, Z) = (37.6, -6)$ (indicated by green diamond marks in Figure 7a) as the flux rope passes by. Due to the O-point structure, there is a bump in B_R around 334 μs as shown in Figure 7b. B_R is supposed to have the minimum variance without the O-point. The transformation matrix produced by MVAB for this case is

$$\begin{pmatrix} x_5 \\ y_5 \\ z_5 \end{pmatrix} = \begin{pmatrix} 0.4401 & 0.8906 & -0.1150 \\ -0.8824 & 0.4052 & -0.2389 \\ -0.1662 & 0.2066 & 0.9642 \end{pmatrix} \begin{pmatrix} R \\ Y \\ Z \end{pmatrix}.$$
(9)

Again, MVAB fails to predict a proper unit vector normal to the current sheet although the three eigenvalues are well-separated as shown in Figure 7c. However, it still produces a reasonable tangential vector as $\hat{\mathbf{z}}_5$ remains close to $\mathbf{e}_Z$.

[22] These examples show that MVAB generally does not produce a proper normal vector even if the current sheet structure does not undergo significant time variations. However, MVAB is much better for determining the direction of the reconnecting magnetic field, the maximum-varying component, which agrees with *Mozer and Retinó* [2007]. MVAB's prediction for $\hat{\mathbf{z}}$ is better for measurement points close to the X-point since variations of the other two components are smaller there.

4. Boundary-Crossing Time Analysis

[23] Since *Russell et al.* [1983] first presented a four-spacecraft analysis technique which can decide the normal vector, speed, and thickness of a boundary based on the boundary-crossing time of each spacecraft, many different methods based on different assumptions have been developed. The common assumption of all BCTA techniques is that the boundary is a 1-D plane. The original BCTA by *Russell et al.* [1983] is called the Constant Velocity Approach (CVA) because it assumes V_n is a constant during the crossing. By noting that the assumption of a constant velocity may not be proper for current sheets in the magnetopause, *Haaland et al.* [2004] develop the Constant Thickness Approach (CTA) where the width of the boundary is assumed to be a constant but V_n a cubic polynomial of time. In another method called the Discontinuity Analyzer (DA) [*Dunlop and Woodward*, 1998], both the thickness and the velocity can be varied but the normal vector $\hat{\mathbf{n}}$ has to be
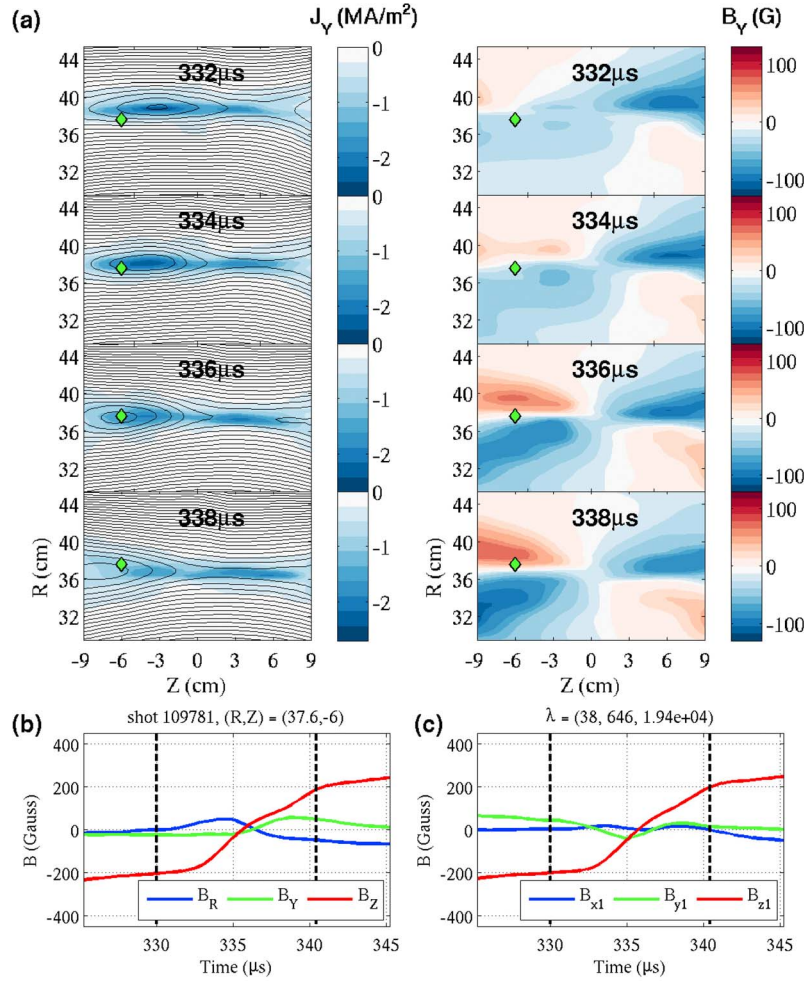
Figure 7. (a) (left) 2-D profiles of J_Y (color) with contours of Ψ of a discharge containing a flux rope. A clear O-point related to the high local current density is formed and ejected downstream. (right) 2-D profiles of B_Y. Initially, the left side of the quadrupolar structure is destroyed due to the development of the O-point structure ('flux rope'). As the flux rope is ejected downstream, the quadrupolar structure is recovered. The green diamond marks indicate the location of the sample measurement point for data shown in Figure 7b. (b) Magnetic field data at a sample measurement point at $(R, Z) = (37.6, -6)$. The bump in the normal component B_R is caused by the passing of the flux rope. (c) The same data after being transformed into the (x, y, z) coordinate system suggested by MVAB. Three eigenvalues are shown above the panel. Even though three eigenvalues are well-separated for this case, the (x, y, z) coordinate system constructed by MVAB is far from the real magnetic geometry.

obtained from single-spacecraft analysis such as MVAB. Finally, the Minimum Thickness Variation (MTV) method has been developed by combining all of the above three methods [*Paschmann et al.*, 2005]. MTV can be considered as an improved version of DA since it does not require single-spacecraft techniques. Instead, it uses CVA and CTA to find $\hat{\mathbf{n}}$, and the velocity is modeled as a cubic polynomial of time rather than a quadratic as in DA.

4.1. BCTA Results and Analysis: 2D Case

[24] We now apply CVA, CTA, and MTV to data from the MRX jogging experiments to see whether they predict a proper $\hat{\mathbf{n}}$, V_n, and current sheet thickness δ_{CS}. Data from the same discharge shown in Figures 4, 5, and 6 is used. We choose three test measurement points $((R, Z) = (38.5, -3)$,

(38.5, 3), and (33.7, 0); $Y = 0$ for all) that form a nearly equilateral triangle in the main measurement plane with leg length ~ 6 cm. One more measurement point is provided by an additional probe at $(R, Y, Z) = (36.5, -9, 0)$. Figures 8a and 8b show the location of the four measurement points: $\mathbf{r}_1$, $\mathbf{r}_2$, $\mathbf{r}_3$, and $\mathbf{r}_4$. The location of $\mathbf{r}_1$ marked by a red diamond is actually 9 cm below of the plane. Thus, these measurement points form a tetrahedron with the fourth point at $Y = -9$ cm approximately 10 cm from the others. The upstream density measured by a Langmuir probe for this discharge is about 4×10^{13} cm^{-3}, which leads to an ion skin depth of $\delta_i \equiv c/\omega_{pi} \approx 5.1$ cm for this deuterium plasma. Thus, the separation between measurement points is comparable to δ_i.
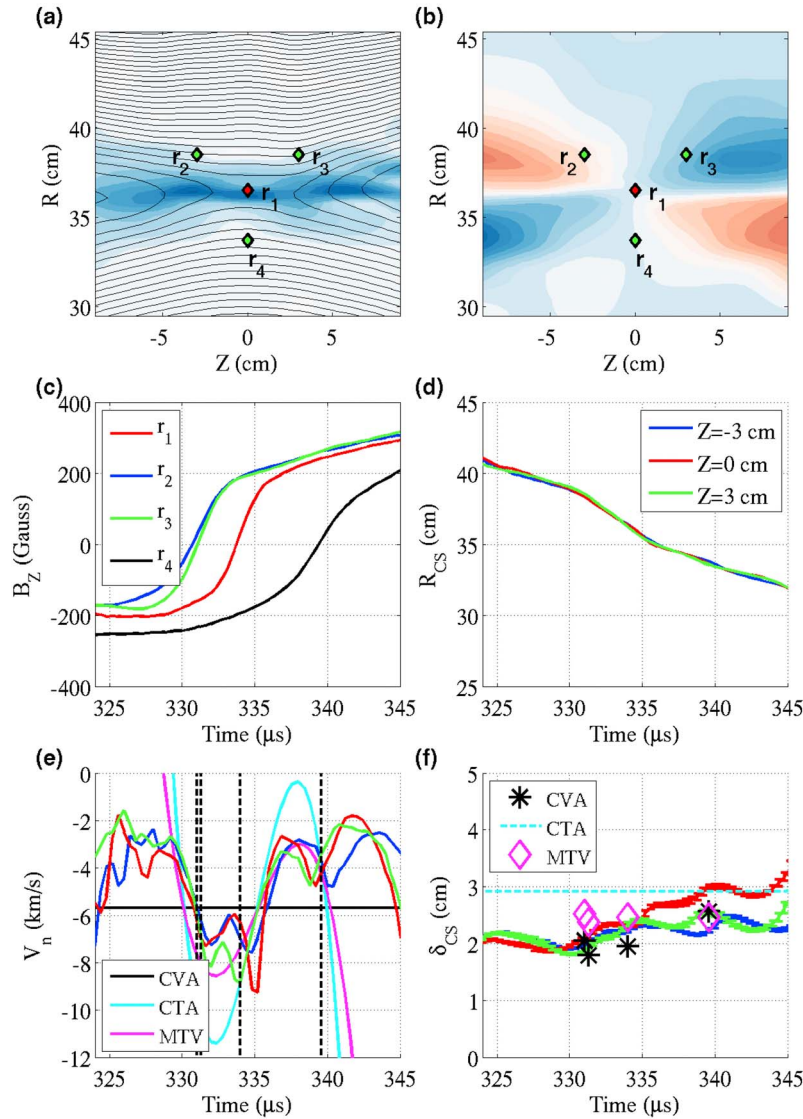
Figure 8. (a) Profile of J_Y with contours of Ψ of the discharge 114338 when the $B_Z = 0$ boundary is close to $\mathbf{r}_1$. (b) That of B_T. Four measurement points ($\mathbf{r}_1$, $\mathbf{r}_2$, $\mathbf{r}_3$, and $\mathbf{r}_4$) used for BCTA are shown in both panels. Those measurement points form a tetrahedron since $\mathbf{r}_1$, which is indicated by the red diamond mark, is actually 9 cm below of the main measurement plane. Color scales are the same as in Figure 4. (c) Reconnecting magnetic field B_Z profiles at 4 sample measurement points for BCTA. The location of the measurement points in (R, Y, Z) coordinates is $\mathbf{r}_1 = (36.5, -9, 0)$, $\mathbf{r}_2 = (38.5, 0, -3)$, $\mathbf{r}_3 = (38.5, 0, 3)$, and $\mathbf{r}_4 = (33.7, 0, 0)$, respectively. (d) Current sheet radial location R_{CS} measured by magnetic probe arrays at $Z = -3$, 0, and 3 cm. (e) Normal velocity V_n from CVA, CTA, and MTV. The red, blue, and green curves are radial velocities of the current sheet (dR_{CS}/dt) at $Z = -3$, 0, and 3 cm, respectively. (f) Current sheet width δ_{CS} from CVA, CTA, and MTV. The red, blue, and green curves stand for measured δ_{CS} at $Z = -3$, 0, and 3 cm, respectively.

[25] Figure 8c shows B_Z at each measurement point. These time profiles are fitted to the following Harris-type function:

$$B_Z(t) = B_a + B_m \tanh\left[\frac{t - t_i}{\tau_i}\right] + C_B(t - t_i). \qquad (10)$$

The third term is required to take the field from external coils such as the PF and equilibrium field coils into account. Following *Haaland et al.* [2004], t_i is the crossing time and τ_i is half of the crossing duration for i-th measurement point.

[26] With these crossing times and durations, CVA and CTA are performed to find the normal vector $\hat{\mathbf{n}}$. The normal vector from CVA for this example is $\hat{\mathbf{n}} = 0.9987\mathbf{e}_R - 0.0435\mathbf{e}_Y - 0.0260\mathbf{e}_Z$ and that from CTA is $\hat{\mathbf{n}} = 0.9923\mathbf{e}_R + 0.1147\mathbf{e}_Y - 0.0460\mathbf{e}_Z$. Both normal vectors are close to the reference normal $\mathbf{e}_R$. The normal vector used for MTV is just the renormalized average over the above two normal vectors.

[27] By fitting radial B_Z profiles from the 2-D magnetic probe arrays into a similar Harris-type function of equation (10),

the radial current sheet location R_{CS} and width δ_{CS} are determined independently. Figure 8d shows R_{CS} at $Z = -3$ cm (the same Z location of $\mathbf{r}_2$), at $Z = 0$ cm ($\mathbf{r}_1$ and $\mathbf{r}_4$), and at $Z = 3$ cm ($\mathbf{r}_3$), from which the radial velocity of the current sheet can be computed as shown in Figure 8e (blue, red, green curves). Black dashed vertical lines indicate four crossing times (t_i). These measured values can be compared to estimates from CVA, CTA, and MTV. The black horizontal line in Figure 8e indicates the constant V_n from CVA of -5.71 km/s. Average radial velocities over crossing times measured at $Z = -3, 0$, and 3 cm are $-5.32, -5.51$, and -5.80 km/s, respectively. The cyan curve in the same figure is $V_n(t)$ from CTA, which is not in quantitative agreement with measured values as the change of velocity is exaggerated. The result from MTV (magenta curve) better describes the actual change of the current sheet velocity during crossings. This is because δ_{CS} is also allowed to vary in MTV and δ_{CS} is actually changing as shown in Figure 8f. Again, the red, blue, green curves are results from the Harris fitting and error bars represent uncertainties in the fitting. δ_{CS} from CVA (black asterisks) is both qualitatively and quantitatively in agreement with the measured values. On the other hand, the thickness from CTA is 2.92 cm, which is generally higher than the globally measured values. The values from MTV is quantitatively all right, but does not show the tendency of increasing δ_{CS} at $Z = 0$ (red curve) at later times.

[28] The results from CVA are surprisingly close to the measured values even though the radial current sheet velocity varies from -8 to -3 km/s during the crossing as shown in Figure 8e. Although the magnitude of the current sheet velocity is changing, its direction remains radial, so that the differences of crossing times by radial separations are still dominant. Furthermore, CVA is not sensitive to changes in the instantaneous velocity. As long as the average velocity over t_i to t_{i+1} does not change much, we can expect reasonable results from CVA. However, the change of instantaneous velocity does affect the reliability of results from the Harris fitting by disrupting the time profile of the maximum varying magnetic field component B_Z. When some of the Harris fittings are poor, we find that normal vectors from CVA can be improved by taking the zero-crossing time of B_Z as the crossing time t_i.

[29] The results from CTA are sensitive to the assumption of constant current sheet thickness. In this example, δ_{CS} changes over time especially at $Z = 0$ where both $\mathbf{r}_1$ and $\mathbf{r}_4$ exist. The coefficients of the higher order terms of $V_n(t)$ become considerable due to the small changes in thickness, exaggerating the change in V_n. CTA is also sensitive to τ_i from the Harris fitting; small uncertainties in τ_i can significantly alter CTA results. In most of the cases we have tested, the normal vector $\hat{\mathbf{n}}$ from CTA is reasonable but $V_n(t)$ and δ_{CS} from CTA do not agree well with measured values.

[30] MTV produces better results than CTA especially for $V_n(t)$. However, δ_{CS} from MTV is sometimes far from measured values. Moreover, MTV is generally unsuccessful in reflecting the actual change in δ_{CS}, which is anticipated because MTV minimizes the variance of δ_{CS}.

4.2. BCTA Results and Analysis: 3D Case

[31] We have also tested BCTA techniques on data from discharges that undergo significant temporal changes caused by 3-D structures. Figure 9a shows the time evolution of J_Y with contours of Ψ and B_Y. At $t = 330$ μs, the position of the main X-point is near $Z = 0$ based on the quadrupole B_Y structure. An O-point is formed near $Z = -3$ cm, generating another X-point probably near $Z = -11$ cm outside of the measurement window. As shown in Figure 9b, the $B_Z = 0$ boundary passes $\mathbf{r}_1 = (36.5, -9, 0)$ much earlier than $\mathbf{r}_5 = (36.4, 0, 0)$, indicating considerable toroidal asymmetry. This flux rope dynamically evolves, changing the magnetic geometry significantly. As it moves toward the $+Z$ direction, the original X-point is pushed toward the same direction and the center of the quadrupolar B_Y structure is shifted to around $Z = -9$ cm, close to the second X-point, which means the most active X-point is now at $Z = -9$ cm.

[32] The normal vector from CVA is $\hat{\mathbf{n}} = 0.9816\mathbf{e}_R - 0.1906\mathbf{e}_Y + 0.0089\mathbf{e}_Z$ and the normal velocity is -5.87 km/s. $\hat{\mathbf{n}}$ has a sizable $\mathbf{e}_Y$ component due to the toroidal asymmetry probably caused by kink-type instability along the out-of-plane current direction. As shown in Figure 9d, the radial velocity of the current sheet (blue, red, and green curves) remains relatively steady and V_n from CVA agrees with the average radial velocity during crossings which is -5.81 km/s at $Z = 0$. δ_{CS} from CVA is also in agreement with measured values as shown in Figure 9e. Since the radial velocity is decreasing, δ_{CS} for the last crossing at $\mathbf{r}_4$ is estimated to be higher than the measured value at $Z = 0$.

[33] CTA also produces a reasonable normal vector for this case, which is $\hat{\mathbf{n}} = 0.9686\mathbf{e}_R - 0.2485\mathbf{e}_Y + 0.0110\mathbf{e}_Z$. However, the $V_n(t)$ from CTA is totally deviated from the measured radial velocity profile as shown in Figure 9d. In this example, the first three crossing times are very close to each other (see the black dashed vertical lines). The durations of the crossings, on the other hand, are diverse since δ_{CS} at different axial locations is actually different due to the flux lope formation. To make the current sheet width for each crossing the same, $V_n(t)$ has to change quickly, so that the coefficients of the higher order terms become unrealistically large. In MTV, $V_n(t)$ is again better than CVA, but the estimated δ_{CS} is too small in this case.

5. Synthesis of Results

5.1. MVAB and BCTA

[34] To compare the results of BCTA with those of MVAB, we perform MVAB for data from the same measurement points as used in section 4.1. Table 1 summarizes MVAB results which have similar trends to those described in section 3. First, the normal suggested vector $\mathbf{u}_1$ is close to the reference normal $\mathbf{e}_R$ at $Z = \pm 3$ ($\mathbf{r}_2$ and $\mathbf{r}_3$) but it becomes a mixture of $\mathbf{e}_Y$ and $\mathbf{e}_R$ at $Z = 0$ ($\mathbf{r}_1$ and $\mathbf{r}_4$). Second, MVAB determines the direction of the reconnecting field component well at $Z = 0$, but at $Z = \pm 3$, $\mathbf{u}_3$ is degraded as the Hall field cannot be distinguished from the reconnecting field.

[35] A fundamental reason that MVAB sometimes fails to determine a proper normal vector is that the X-line magnetic geometry inherently has a 2-D structure. Let us explain this under the idealized 2-D X-line geometry shown in Figure 10. The boundary of $\partial B_x/\partial x = 0$ coincides with the current sheet location at $x = 0$ and extends along the normal direction ($\hat{\mathbf{x}}$) only at $z = 0$. Because MVAB requires a finite number of samples of data around the boundary, at $z \neq 0$, it naturally
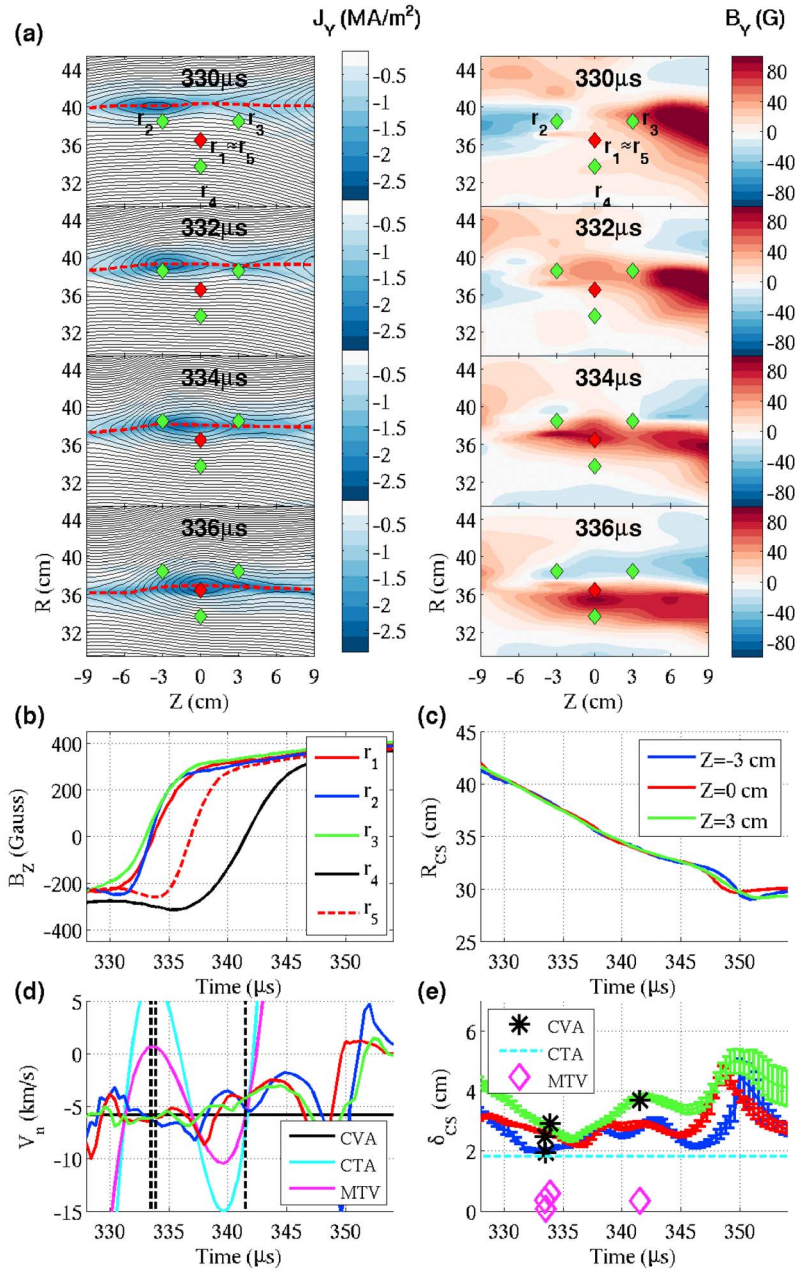
Figure 9. BCTA for the discharge 114332 which has a 'flux rope' structure. (a) (left) 2-D profiles of J_Y (color) with contours of ψ. Red dashed lines stand for the $B_Z = 0$ boundary. (right) Those of B_Y. A clear O-point is formed and moves to the $+Z$ direction changing magnetic geometry. The location of the measurement points is indicated by green and red diamonds. $\mathbf{r}_1$ and $\mathbf{r}_5$ has the same Z location and a similar R location, but $\mathbf{r}_1$ is located 9 cm below of the main measurement plane. (b) Reconnecting magnetic field B_Z profiles at sample measurement points of $\mathbf{r}_1 = (36.5, -9, 0)$, $\mathbf{r}_2 = (38.5, 0, -3)$, $\mathbf{r}_3 = (38.5, 0, 3)$, $\mathbf{r}_4 = (33.7, 0, 0)$, and $\mathbf{r}_5 = (36.4, 0, 0)$ in (R, Y, Z). Although $\mathbf{r}_1$ and $\mathbf{r}_5$ have a similar radial position, the $B_Z = 0$ surface crosses $\mathbf{r}_1$ much earlier, which is a sign of toroidal asymmetry of this discharge. (c) Current sheet radial location R_{CS} measured by magnetic probe arrays at $Z = -3$, 0, and 3 cm. (d) Normal velocity V_n from CVA, CTA, and MTV. The red, blue, and green curves are radial velocities of the current sheet (dR_{CS}/dt) at $Z = -3$, 0, and 3 cm, respectively. (e) Current sheet width δ_{CS} from CVA, CTA, and MTV. The red, blue, and green curves stand for measured δ_{CS} at $Z = -3$, 0, and 3 cm, respectively.

includes data from the region where $\partial B_x/\partial x = 0$ is not satisfied. Even at $Z = 0$, the variance of B_x is not guaranteed to be minimal since $\partial B_y/\partial x$ is also zero there. Actually, more than 50 percent of the tested cases for

MRX jog experiment data at $Z = 0$ are degenerate ($\lambda_1 \sim \lambda_2$) since neither B_R nor B_Y changes much.

[36] The results in Figure 6 support this idea. As shown in Figure 6a, at $Z = 0$ in the vicinity of the X point, the length of

Table 1. MVAB Results for Data From the Same Sample Measurement Points Used for BCTA in Figure 8[a]

Location	$\mathbf{u}_1$ (R,Y,Z)	$\mathbf{u}_3$ (R,Y,Z)	Eigenvalues
$\mathbf{r}_1$	(0.8871, 0.4612, 0.0182)	(−0.0288, 0.0159, 0.9995)	3, 19, 2.07 × 10⁴
$\mathbf{r}_2$	(0.9983, −0.0452, −0.0374)	(0.0501, 0.3226, 0.9452)	1, 47, 1.37 × 10⁴
$\mathbf{r}_3$	(0.9964, −0.0741, −0.0401)	(0.0149, −0.3134, 0.9495)	0.2, 23, 1.80 × 10⁴
$\mathbf{r}_4$	(0.1002, −0.9942, −0.0388)	(−0.0056, 0.0395, 0.9992)	0.2, 3, 1.35 × 10⁴

[a]The variable $\mathbf{u}_1$ is the suggested normal vector and the variable $\mathbf{u}_3$ is the suggested direction of the reconnecting field.

the error bars becomes smaller with a large nest size M, which is expected by equations (7) and (8). On the other hand, the error bars do not change much at $Z \neq 0$. This is because the smallest eigenvalue λ_1 becomes larger as M increases, indicating the source of the variance is not from random noise but from something systematic; the magnetic geometry is not 1-D. With a larger data sample size, more data points lie in the region where $\partial B_x/\partial x \neq 0$, increasing the variance λ_1.

[37] CVA, on the other hand, estimates $\hat{\mathbf{n}}$ based on the moment that the boundary passes the measurement point. Therefore, as long as the boundary is close to a plane and V_n is approximately constant over time, it produces a reasonable $\hat{\mathbf{n}}$ and V_n. As shown in Figure 10, the $B_z = 0$ boundary that coincides with the location of the current sheet center is a straight line (a plane in 3-D) in spite of the 2-D X-line magnetic geometry. This is why crossing time analysis works even for discharges with flux ropes like Figure 9. As shown in Figure 9a, red dashed lines ($B_Z = 0$ boundaries) remain close to a straight line especially between $Z = \pm 3$ cm where crossing time analysis is employed.

[38] Another reason for BCTA's better performance is that BCTA utilizes the maximum-varying magnetic field component (B_z), while MVAB minimizes the small normal component (B_x). Thus, MVAB is more vulnerable to noise and temporal changes than BCTA. The example shown in Figure 7 supports that the temporal change in the magnetic geometry can severely affect MVAB results.

5.2. Hybrid Technique for Magnetic Geometry Determination

[39] We have confirmed that the normal vector from BCTA is more reliable than that from MVAB. One disadvantage of BCTA is that it cannot differentiate the two tangential vectors. MVAB, on the other hand, is robust in estimating the direction of the reconnecting magnetic field especially in the vicinity of the X-point where the Hall field is small. Thus, the local magnetic geometry can be precisely determined by appropriately combining two methods.

[40] We suggest the following procedure for the determination of the local magnetic geometry when four spacecraft pass through a current sheet layer. First, employ MVAB for all spacecraft data. Decide which spacecraft is closest to the X-point by either looking at other data such as the ion velocity or comparing λ_1 and λ_2 for each spacecraft. The one that has the smallest sum of λ_1 and λ_2 is mostly likely to be closest to the X-point. $\mathbf{u}_3$ from that spacecraft is a valid indicator for $\hat{\mathbf{z}}$ and this is a temporary direction for the reconnecting magnetic field, $\hat{\mathbf{z}}'$. Find the time evolution of $B_{z'} = \mathbf{B} \cdot \hat{\mathbf{z}}'$ for each spacecraft. Then, estimate $\hat{\mathbf{n}} = \hat{\mathbf{x}}$ and V_n by crossing time analysis such as CVA. Since $\hat{\mathbf{n}}$ and $\hat{\mathbf{z}}'$ may not be orthogonal, decide $\hat{\mathbf{y}}$ first from $\hat{\mathbf{y}} = \hat{\mathbf{z}}' \times \hat{\mathbf{x}}$. Finally, $\hat{\mathbf{z}}$

is given by $\hat{\mathbf{z}} = \hat{\mathbf{x}} \times \hat{\mathbf{y}}$. The transformation matrix obtained by this procedure for data from the discharge 114338 is

$$\begin{pmatrix} x \\ y \\ z \end{pmatrix} = \begin{pmatrix} 0.9987 & -0.0435 & -0.0260 \\ 0.0430 & 0.9969 & -0.0147 \\ 0.0266 & 0.0135 & 0.9975 \end{pmatrix} \begin{pmatrix} R \\ Y \\ Z \end{pmatrix}, \quad (11)$$

which is very close to the desired identity matrix.

6. Summary and Discussion

[41] We have tested various techniques for determining the boundary normal direction in space with the use of data from the MRX jog experiment. Multispacecraft BCTA techniques are more successful in estimating $\hat{\mathbf{n}}$ than the single-spacecraft method, MVAB. MVAB deduces the direction of the maximum varying reconnecting magnetic field well. The suggested $\hat{\mathbf{z}}$ is best in the vicinity of the X-point since the effect from the Hall field is smallest there. Thus, the complete local magnetic geometry can be decided by using BCTA to find the normal vector $\hat{\mathbf{n}}$ and by employing MVAB to estimate $\hat{\mathbf{z}}$. This hybrid procedure is presented in section 5.2.

[42] The better performance of BCTA over MVAB in estimating $\hat{\mathbf{n}}$ comes from the following reasons. First,
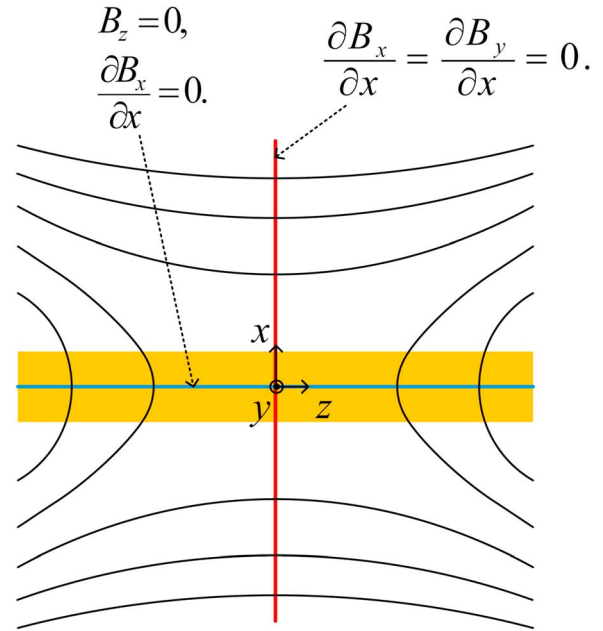

Figure 10. Idealized X-line geometry. The orange box illustrates the current sheet. The blue line is the boundary of $B_z = 0$ where $\partial B_x/\partial x = 0$ is satisfied. The $\partial B_x/\partial x = 0$ extends along the x direction only at $z = 0$ (red line), where $\partial B_y/\partial x = 0$ is also satisfied there.

the reconnecting current sheet layer fundamentally has 2-D or 3-D structures, which often makes results of MVAB unreliable. Even though the X-line magnetic geometry is 2-D or 3-D, the current sheet itself can be close to a plane as shown in Figure 10. BCTA, in this case, can successfully estimate the normal vector. Second, BCTA has more immunity to noise and/or temporal changes since it utilizes the large magnetic field component B_z while MVAB has to rely on the smaller normal component B_x.

[43] Among BCTA techniques, the performance of CVA is more robust than both CTA and MTV for MRX jogging data. For CVA, the velocity of the boundary along the normal vector V_n and the current sheet width δ_{CS} are in agreement with the measured values by the 2-D magnetic probe arrays. CTA is more sensitive to the validity of its basic assumption; results of CTA are deviated from the measured values when the current sheet thickness is changing over space and/or time. MTV estimates the instantaneous normal velocity profile $V_n(t)$ generally better than CTA but it does not reflect the actual variance of δ_{CS}. In cases where the constant thickness assumption is quite valid, $V_n(t)$ can be further improved by applying MTV. One of the major sources of errors of these BCTA techniques is uncertainties in t_i and τ_i from the Harris fitting. CTA and MTV are more sensitive to these errors than CVA.

[44] These results do not necessarily mean CVA is a better method than CTA and MTV. Results from CVA may not be reliable when the current sheet experiences significant acceleration between each crossing. If the spacing between spacecraft is much smaller than the system scale such that the constant thickness assumption is valid, then CTA and MTV should be better choices over CVA. In MRX jogging experiment, because the system size is not much greater than the separation of sample measurement points and the current sheet width changes over space and time, $V_n(t)$ from CTA and MTV does not reflect the actual normal speed of the boundary.

[45] For BCTA, the distance between measurement points (or spacecraft) is important. If the separation is too small, the normal vector only reflects the local geometry that can be different from the global geometry due to, for example, flux ropes and/or kinked current sheets. If it is too large, the basic assumption of the boundary being a plane may not be satisfied. Moreover, V_n may not be considered to be a constant. For the MRX jog experiment, separation of $(1-2)\delta_i$ is proper because our system size is about $10\delta_i$ and the characteristic spatial scale of the kinked current sheet structure along toroidal direction is also expected to be comparable to the ion skin depth.

[46] In the future, we plan to perform a more detailed laboratory test of spacecraft data analysis techniques by systematically changing the separation of measurement points from the electron skin depth scale (order of mm) like that in the MMS mission to the ion skin depth scale. In addition, change along the out-of-plane direction will be better monitored by placing multiple probes along the symmetric direction.

References

Angelopoulos, V., et al. (2008), Tail reconnection triggering substorm onset, *Science*, *321*, 931–935, doi:10.1126/science.1160495.

Bauer, T. M., M. W. Dunlop, B. U. O. Sonnerup, N. Sckopke, A. N. Fazakerley, and A. V. Khrabrov (2000), Dual spacecraft determinations of magnetopause motion, *Geophys. Res. Lett.*, *27*, 1835–1838, doi:10.1029/2000GL000041.

Berchem, J., and C. T. Russell (1982), The thickness of the magnetopause current layer: ISEE 1 and 2 observations, *J. Geophys. Res.*, *87*, 2108–2114, doi:10.1029/JA087iA04p02108.

Dorfman, S. E. (2011), Experimental study of 3-D, impulsive reconnection events in a laboratory plasma, PhD thesis, Dep. of Astrophys. Sci., Princeton Univ., Princeton, N. J.

Dunlop, M. W., and T. I. Woodward (1998), Multi-spacecraft discontinuity analysis: Orientation and motion, in *Analysis Methods for Multi-spacecraft Data*, edited by G. Paschmann and P. W. Daly, pp. 271–306, Eur. Space Agency, Noordwijk, Netherlands.

Eastwood, J. P., D. G. Sibeck, J. A. Slavin, M. L. Goldstein, B. Lavraud, M. Sitnov, S. Imber, A. Balogh, E. A. Lucek, and I. Dandouras (2005), Observations of multiple X-line structure in the Earth's magnetotail current sheet: A Cluster case study, *Geophys. Res. Lett.*, *32*, L11105, doi:10.1029/2005GL022509.

Eastwood, J. P., T.-D. Phan, F. S. Mozer, M. A. Shay, M. Fujimoto, A. Retinò, M. Hesse, A. Balogh, E. A. Lucek, and I. Dandouras (2007), Multi-point observations of the Hall electromagnetic field and secondary island formation during magnetic reconnection, *J. Geophys. Res.*, *112*, A06235, doi:10.1029/2006JA012158.

Haaland, S. E., et al. (2004), Four-spacecraft determination of magnetopause orientation, motion and thickness: Comparison with results from single-spacecraft methods, *Ann. Geophys.*, *22*, 1347–1365, doi:10.5194/angeo-22-1347-2004.

Harris, E. G. (1962), On a plasma sheath separating regions of oppositely directed magnetic field, *Nuovo Cimento*, *23*, 115–121, doi:10.1007/BF02733547.

Ji, H., M. Yamada, S. Hsu, R. Kulsrud, T. Carter, and S. Zaharia (1999), Magnetic reconnection with Sweet-Parker characteristics in two-dimensional laboratory plasmas, *Phys. Plasmas*, *6*, 1743, doi:10.1063/1.873432.

Khotyaintsev, Y. V., A. Vaivads, A. Retinò, M. André, C. J. Owen, and H. Nilsson (2006), Formation of inner structure of a reconnection separatrix region, *Phys. Rev. Lett.*, *97*, 205003, doi:10.1103/PhysRevLett.97.205003.

Khrabrov, A. V., and B. U. Ö. Sonnerup (1998a), Orientation and motion of current layers: Minimization of the Faraday residue, *Geophys. Res. Lett.*, *25*, 2373–2376, doi:10.1029/98GL51784.

Khrabrov, A. V., and B. U. Ö. Sonnerup (1998b), Error estimates for minimum variance analysis, *J. Geophys. Res.*, *103*, 6641–6651, doi:10.1029/97JA03731.

Mozer, F. S., and A. Retinò (2007), Quantitative estimates of magnetic field reconnection properties from electric and magnetic field measurements, *J. Geophys. Res.*, *112*, A10206, doi:10.1029/2007JA012406.

Mozer, F. S., S. D. Bale, and T. D. Phan (2002), Evidence of diffusion regions at a subsolar magnetopause crossing, *Phys. Rev. Lett.*, *89*, 015002, doi:10.1103/PhysRevLett.89.015002.

Øieroset, M., T.-D. Phan, M. Fujimoto, R. P. Lin, and R. P. Lepping (2001), In situ detection of collisionless reconnection in the Earth's magnetotail, *Nature*, *412*, 414–417, doi:10.1038/35086520.

Paschmann, G., B. U. Ö. Sonnerup, I. Papamastorakis, N. Sckopke, G. Haerendel, S. J. Bame, J. R. Asbridge, J. T. Gosling, C. T. Russell, R. C. Elphic (1979), Plasma acceleration at the earth's magnetopause: Evidence for reconnection, *Nature*, *282*, 243–246, doi:10.1038/282243a0.

Paschmann, G., B. U. Ö. Sonnerup, I. Papamastorakis, W. Baumjohann, N. Schopke, and H. Lühr (1990), The magnetopause and boundary layer for small magnetic shear: Convection electric fields and reconnection, *Geophys. Res. Lett.*, *17*, 1829–1832, doi:10.1029/GL017i011p01829.

Paschmann, G., S. Haaland, B. U. Ö. Sonnerup, H. Hasegawa, E. Georgescu, B. Klecker, T. D. Phan, H. Rème, and A. Vaivads (2005), Characteristics of the near-tail dawn magnetopause and boundary layer, *Ann. Geophys.*, *23*, 1481–1497, doi:10.5194/angeo-23-1481-2005.

Phan, T. D., et al. (2000), Extended magnetic reconnection at the Earth's magnetopause from detection of bi-directional jets, *Nature*, *404*, 848–850, doi:10.1038/35009050.

Phan, T. D., et al. (2006), A magnetic reconnection X-line extending more than 390 Earth radii in the solar wind, *Nature*, *439*, 175–178, doi:10.1038/nature04393.

Ren Y., M. Yamada, H. Ji, S. Dorfman, S. P. Gerhardt, and R. Kulsrud (2008), Experimental study of the Hall effect and electron diffusion region during magnetic reconnection in a laboratory plasma, *Phys. Plasmas*, *15*, 082113, doi:10.1063/1.2936269.

Retinó, A., D. Sundkvist, A. Vaivads, F. Mozer, M. Andre, and C. J. Owen (2007), In situ evidence of magnetic reconnection in turbulent plasma, *Nature Phys.*, *3*, 235–238, doi:10.1038/nphys574.

Retinó, A., et al. (2008), Cluster observations of energetic electrons and electromagnetic fields within a reconnecting thin current sheet in the Earth's magnetotail, *J. Geophys. Res.*, *113*, A12215, doi:10.1029/2008JA013511.

Rosenqvist, L., A. Vaivads, A. Retino, T. Phan, H. J. Opgenoorth, I. Dandouras, and S. Buchert (2008), Modulated reconnection rate and energy conversion at the magnetopause under steady IMF conditions, *Geophys. Res. Lett.*, *35*, L08104, doi:10.1029/2007GL032868.

Russell, C. T., M. M. Mellott, E. J. Smith, and J. H. King (1983), Multiple spacecraft observations of interplanetary shocks: Four spacecraft determination of shock normals, *J. Geophys. Res.*, *88*, 4739–4748, doi:10.1029/JA088iA06p04739.

Sonnerup, B. U. Ö., and L. J. Cahill (1967), Magnetopause structure and attitude from Explorer 12 observations, *J. Geophys. Res.*, *72*, 171–183, doi:10.1029/JZ072i001p00171.

Sonnerup, B. U. Ö., and M. Scheible (1998), Minimum and maximum variance analysis, in *Analysis Methods for Multi-spacecraft Data*, edited by G. Paschmann and P. W. Daly, pp. 185–220, Eur. Space Agency, Noordwijk, Netherlands.

Sonnerup, B. U. Ö., I. Papamastorakis, G. Paschmann, and H. Lühr (1987), Magnetopause properties from AMPTE/IRM observations of the convection electric field: Method development, *J. Geophys. Res.*, *92*, 12,137–12,159, doi:10.1029/JA092iA11p12137.

Terasawa, T., et al. (1996), On the determination of a moving MHD structure: Minimization of the residue of integrated Faraday's equation, *J. Geomagn. Geoelectr.*, *48*, 603–614.

Vaivads, A., Y. Khotyaintsev, M. André, A. Retinò, S. C. Buchert, B. N. Rogers, P. Décréau, G. Paschmann, and T. D. Phan (2004), Structure of the magnetic reconnection diffusion region from four-spacecraft observations, *Phys. Rev. Lett.*, *93*, 105001, doi:10.1103/PhysRevLett.93.105001.

Yamada, M. (2007), Progress in understanding magnetic reconnection in laboratory and space astrophysical plasmas, *Phys. Plasmas*, *14*, 058102, doi:10.1063/1.2740595.

Yamada, M., H. P. Furth, W. Hsu, A. Janos, S. Jardin, M. Okabayashi, J. Sinnis, T. H. Stix, and K. Yamazaki (1981), Quasistatic formation of the spheromak plasma configuration, *Phys. Rev. Lett.*, *4*, 188–191, 10.1103/PhysRevLett.46.188.

Yamada, M., H. Ji, S. Hsu, T. Carter, R. Kulsrud, N. Bretz, F. Jobes, Y. Ono, and F. Perkins (1997), Study of driven magnetic reconnection in a laboratory plasma, *Phys. Plasmas*, *4*, 1936, doi:10.1063/1.872336.

Yamada, M., R. Kulsrud, and H. Ji (2010), Magnetic reconnection, *Rev. Mod. Phys.*, *82*, 603–664, doi:10.1103/RevModPhys.82.603.

Zweibel, E. G., and M. Yamada (2009), Magnetic reconnection in astrophysical and laboratory plasmas, *Annu. Rev. Astron. Astrophys.*, *47*, 291–332, doi:10.1146/annurev-astro-082708-101726.